79-4036

Mirror Deformation for Phase Compensation of a Thermally Bloomed Laser Beam

David Bushnell* and Jörgen Skogh†
Lockheed Palo Alto Research Laboratory, Palo Alto, Calif.

Under certain conditions phase errors develop over the cross section of an initially coherent beam of electromagnetic radiation propagating through the atmosphere. At the target the beam cross section is therefore enlarged and distorted. This phase error and beam divergence can be partially corrected by insertion of a compensating deformable mirror in the optical system. In this paper the root mean square (rms) error in phase compensation is calculated for a rather thick circular, initially flat mirror deformed by actuators. The inaccuracy in mirror deformations based on a simple thin plate model is evaluated by comparison with results obtained from a more elaborate model in which the mirror is treated as a solid of revolution discretized by means of high-order isoparametric finite elements. It is found that for a given configuration of actuator positions the actuator forces calculated with the two models differ as much as 25%, whereas the predicted rms phase compensation error differs by about 5%. Therefore, the computationally economical thin plate model is used in a parameter study to determine the optimum actuator configuration.

Nomenclature

$a_i, \bar{a}$	= ith actuator force or rigid body motion component; vector a_i, $i = 1, 2, \ldots N+3$
A	= influence function product matrix, Eqs. (5) and (6)
E	= mean-squared phase compensation error, defined in Eq. (4); rms error = $E^{1/2}$
f_{in}	= unit load influence function for ith actuator, n circumferential waves
F	= cross-product vector, Eqs. (5) and (7)
K	= mirror plate flexural rigidity
m	= number of actuator bands
n	= number of circumferential waves
n_{max}	= maximum circumferential wave number used for Fourier expansion
N_D, N_ω	= distortion parameter, beam slew number
N	= number of actuators
P	= Fourier expansion of concentrated load
r	= radial coordinate, Fig. 2
r_i	= radius to ith actuator or actuator band
r_0	= radius of mirror, Fig. 2
R	= range to target
v	= wind velocity normal to the laser beam
$\bar{w}, w$	= normal displacements: solutions of problem of thin circular plate with eccentric concentrated load, Eqs. (20) and (22)
w_{ai}	= normal displacement produced by ith actuator
w_a	= normal displacement produced by actuators and rigid body modes, Eq. (2)
w_c	= normal displacement required to compensate for thermal blooming, Eqs. (1) and (9)
z	= Zernike polynomial, Eqs. (13)
λ	= wavelength of laser beam
ν	= Poisson's ratio
ρ	= r/r_0
θ	= circumferential coordinate, Fig. 2
θ_0	= wind angle, Fig. 2
ω	= laser beam slew rate

Subscripts

i	= ith actuator
n	= number of circumferential waves

Received June 2, 1978; revision received Aug. 24, 1978.

Index category: Structural Design.

*Staff Scientist. Associate Fellow AIAA.
†Staff Scientist.

Introduction

WHEN a uniform laser beam propagates through the atmosphere, it heats the air. If the beam is being slewed, or if there exists a component of wind velocity normal to the beam, the heating is nonuniform across the beam diameter. The nonuniform heating gives rise to gradients in the index of refraction which cause the air within the beam to act as a nonsymmetric lens with aberrations. Thus, the beam focus diverges and becomes distorted, appearing at the target as shown in Fig. 1b, for example. This phenomenon is called thermal blooming. It is possible partially to compensate for this effect by placing a deformable mirror in the beam near the transmitter, as shown in Fig. 1c. The amount that this mirror must be deformed in order to compensate for the thermal blooming of the beam at the target has been predicted by Bradley and Herrmann[1] and this prediction has been verified experimentally by Primmerman and Fouche.[2] Other work on actively controlled optical systems for compensation of atmospheric effects is identified in Ref. 3.

The purpose of this paper is to determine the quality of the optical phase compensation that can be achieved by deformation of a mirror by a set of actuators on its rear surface. The required phase compensation is derived in Ref. 1. The mirror is a circular flat plate with dimensions shown in Fig. 2. The rather large thickness of the mirror is required to absorb heat from the laser beam. In the analysis, the mirror is modeled both with the use of thin plate theory and as a solid of revolution. The measure of quality of optical phase compensation is taken to be the rms difference between the normal surface deflection, as required by the theory of Ref. 1 and the surface deflection caused by the actuators acting on the back of the mirror plate.

Note that if the mirror plate is nonuniformly heated by the laser, it will become distorted due to thermal gradients in and normal to the plane of its surface. The importance of thermal distortion depends on the intensity and uniformity of the laser beam, the amount of heat absorbed by the mirror plate, the efficiency of a mirror cooling system, and the conductivity and coefficient of thermal expansion of the mirror material. Thermal distortion and active compensation for it are beyond the scope of this paper. However, this significant problem

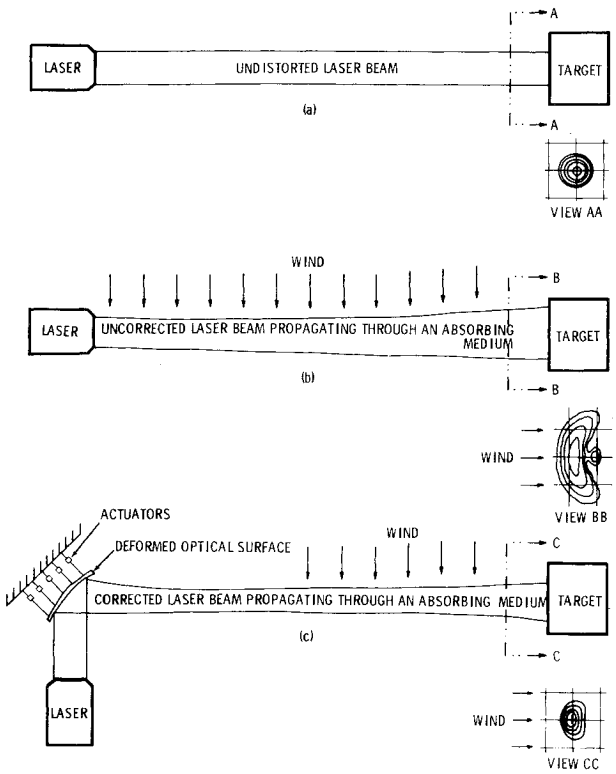

Fig. 1 Thermal blooming: a) Undistorted beam, b) Uncorrected beam in an absorbing medium, c) Beam corrected by deformable mirror.

could be studied via an approach analogous to that presented here.

Finding the Actuator Forces Required to Minimize the rms Phase Compensation Error, $E^{1/2}$

The analysis method is analogous to that described in Refs. 4 and 5. For a specified or "commanded" initial normal surface displacement field $w_c(r,\theta)$ and given the number and locations of actuators (concentrated loads), the actuator forces are determined from the requirement that the mean-squared difference between commanded and actuated surface configurations be minimized.

Let the commanded distortion field $w_c(r,\theta)$ be

$$w_c(r,\theta) = \sum_{n=0}^{n_{\max}} g_n(r)\cos n\theta + \sum_{n=1}^{n_{\max}} h_n(r)\sin n\theta \tag{1}$$

and let the normal displacement field $w_a(r,\theta)$ caused by N actuators (see Fig. 2) be

$$w_a(r,\theta) = \sum_{i=1}^{N+3} a_i \sum_{n=0}^{n_{\max}} f_{in}(r)\cos n(\theta-\theta_i) \tag{2}$$

The functions $f_{in}(r)$, $i=1,2,\ldots N$ represent displacement fields corresponding to unit actuator forces (influence functions). They do not contain rigid body motion components because they are derived from structural models in which axial and circumferential displacements are prevented at $r=r_0$ for $n=0$ and $n=1$ circumferential waves. Therefore, it is necessary to provide these rigid body components as separate influence functions. The upper limit on the summation over i in Eq. (2) is $N+3$ because there are three rigid body modes that affect the normal displacement field: axial displacement, tilt about $\theta=0$ deg, and tilt about $\theta=90$ deg.

The functions $f_{in}(r)$, $i=N+1$, $N+2$, $N+3$, represent unit rigid body modes:

$$f_{(N+1)0}(r)=1;\quad f_{(N+1)n}(r),\quad n=1,2,\ldots n_{\max}=0;\quad \theta_i=0$$

$$f_{(N+2)1}(r)=r/r_0;\ f_{(N+2)n}(r),\quad n=0,2,\ldots n_{\max}=0;\quad \theta_i=0$$

$$f_{(N+3)1}(r)=r/r_0;\ f_{(N+3)n}(r),\quad n=0,2,\ldots n_{\max}=0;\quad \theta_i=\pi/2 \tag{3}$$

Therefore, the multipliers, a_{N+1}, a_{N+2}, a_{N+3} in Eq. (2) represent the amplitudes of rigid body axial displacement, tilt about $\theta=90$ deg, and tilt about $\theta=0$ deg, respectively. The upper limit, $n_{\max}$, is the same for w_c and w_a in order to simplify the computational logic.

If the mean-squared surface configuration compensation error E is defined to be

$$E(a_1,a_2\ldots a_{N+3}) = \frac{1}{\pi r_0^2}\iint (w_c-w_a)^2 r\,dr\,d\theta \tag{4}$$

then minimization of E with respect to the actuator forces a_i, $i=1,2,\ldots N$ and the rigid body motion component amplitudes a_{N+1}, a_{N+2}, a_{N+3} yields a system of $N+3$ linear simultaneous equations

$$A\bar{a}=F \tag{5}$$

in which $\bar{a}$ is the vector containing the actuator force amplitudes and rigid body motion component amplitudes. The (i,k)th element of the matrix A is given by

$$A_{ik} = \pi \sum_{n=1}^{n_{\max}} \left[\int f_{in}(r) f_{kn}(r)\,dr\cos n(\theta_i-\theta_k)\right] + 2\pi\int f_{i0}(r) f_{k0}(r)\,dr \tag{6}$$

and the ith element of the vector F is given by

$$F_i = \pi \sum_{n=1}^{n_{\max}} \int g_n(r) f_{in}(r)\,dr\,\cos n\theta_i + 2\pi\int g_0(r) f_{i0}(r)\,dr + \pi \sum_{n=1}^{n_{\max}} \int h_n(r) f_{in}(r)\,dr\,\sin n\theta_i \tag{7}$$

The solution of Eq. (4) must satisfy three constraint conditions:

Axial force equilibrium:

$$\sum_{i=1}^{N} a_i = 0 \tag{8a}$$

Moment equilibrium about $\theta=0$ deg:

$$\sum_{i=1}^{N} a_i r_i \sin\theta_i = 0 \tag{8b}$$

Moment equilibrium about $\theta=90$ deg:

$$\sum_{i=1}^{N} a_i r_i \cos\theta_i = 0 \tag{8c}$$

These constraint conditions are enforced with the use of the Lagrange multiplier method.

Commanded Distortion $w_c(r,\theta)$

The commanded distortion $w_c(r,\theta)$ derived by Bradley and Herrmann in Ref. 1, has the form

$$w_c(r,\theta) = w_{c0} + w_{c1}\cos(\theta-\theta_0) + w_{c2}\cos 2(\theta-\theta_0) + w_{c3}\cos 3(\theta-\theta_0) \tag{9}$$

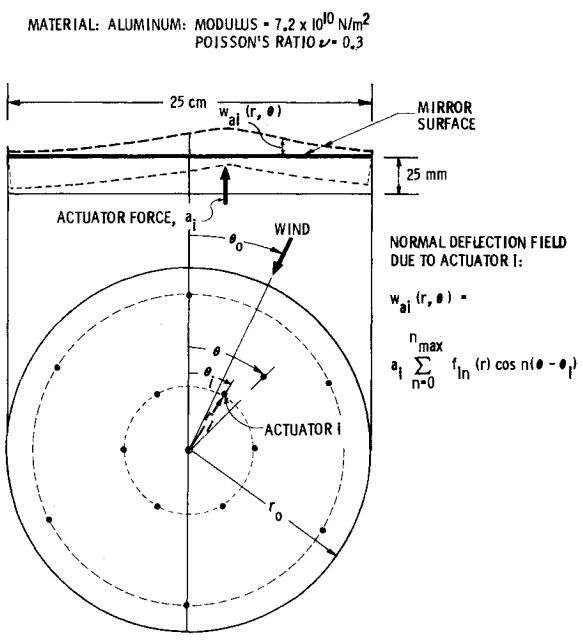

Fig. 2 Circular mirror geometry and actuator bands.

in which θ_0 is the angle of orientation of the commanded distortion relative to the coordinate system used for actuator location (see Fig. 2). Equation (9) can be expressed in the same form as Eq. (1). The coefficients w_{cj}; $j=0, 1, 2, 3$ are given by:

$$w_{c0} \equiv C[A_{20}z(4) + A_{40}z(11) + A_{60}z(22)]$$

$$w_{c1} \equiv C[A_{11}z(2) + A_{31}z(7) + A_{51}z(16)]$$

$$w_{c2} \equiv C[A_{22}z(5) + A_{42}z(12)]$$

$$w_{c3} \equiv C[A_{33}z(9)] \tag{10}$$

where

$$C \equiv \frac{\lambda}{4\pi}\left[\frac{N_D}{2N_\omega}\ell n(1+N_\omega)\right] \tag{11}$$

The quantity N_D is a constant given in Ref. 1 characterizing the magnitude of the change in index of refraction of the gas due to heating and N_ω, the beam slewing number, is:

$$N_\omega = \omega R/v \tag{12}$$

Here ω is the angular velocity of beam slewing, R is the range to the target, and v is the cross-wind velocity. In Eq. (11), λ is the laser radiation wavelength. The quantities $z(i)$ are Zernike polynomials[6] given by

$$z(2)=\rho, \quad z(4)=2\rho^2-1, \quad z(5)=\rho^2, \quad z(7)=3\rho^3-2\rho$$

$$z(9)=\rho^3, \quad z(11)=6\rho^4-6\rho^2+1, \quad z(12)=4\rho^4-3\rho^2$$

$$z(16)=10\rho^5-12\rho^3+3\rho, \quad z(22)=20\rho^6-30\rho^4+12\rho^2-1 \tag{13}$$

where

$$\rho \equiv r/r_0 \tag{14}$$

The coefficients A_{ij} in Eq. (10) are taken from Ref. 1:

$$A_{20}=-0.053 \quad A_{40}=-0.050 \quad A_{60}=+0.021$$

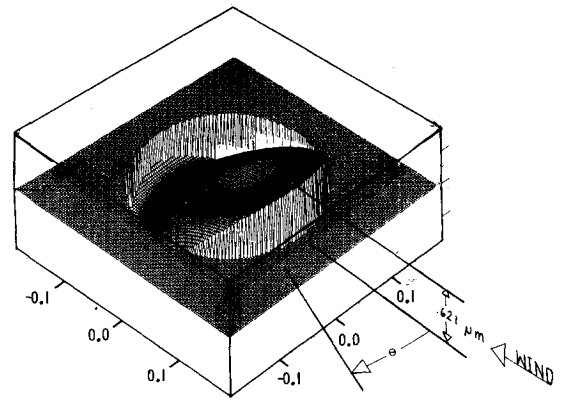

Fig. 3 Normal displacement field w_c required to compensate for thermal blooming under the conditions identified in Eq. (16).

$$A_{11}=+0.440 \quad A_{31}=+0.072 \quad A_{51}=-0.061$$

$$A_{22}=+0.101 \quad A_{42}=+0.096 \quad A_{33}=-0.075 \tag{15}$$

Figure 3 shows the commanded distortion field $w_c(r,\theta)$ for

$$\theta_0=0; \quad \lambda=10.6\mu m; \quad (N_D/2N_\omega)\ell n(1+N_\omega)=1.5 \tag{16}$$

The plot was generated by a routine written by Kohfeld.[7] It can be seen that a major component of the commanded distortion consists of rigid body tilting about $\theta=90$ deg.

Actuated Distortion, $w_a(r,\theta)$

The normal displacement of the mirror surface caused by N actuators is given by Eq. (2). The $f_{in}(r)$, $i=1,2,...N$ are unit load influence functions for the ith actuator and the nth Fourier circumferential harmonic. As in Ref. 4, actuators are considered to be distributed in concentric circular bands, such as is shown in Fig. 2. All actuators on a given band have the same $f_{in}(r)$. Thus, the total number of influence functions which must be calculated is $m \times n_{\max}$, where m is the number of actuator bands, rather than $N \times n_{\max}$, where N is the number of actuators.

The unit load influence functions are generated for each actuator band with the use of two models for the mirror—a thin plate model and a solid-of-revolution model. In both models each actuator is represented by a unit concentrated load acting normal to the mirror at $(r,\theta_i) = (r_i,0)$. The Fourier series expansion of the unit concentrated load is:

$$P_i(\theta) = \frac{1}{2\pi r_i} + \frac{1}{\pi r_i}\sum_{n=1}^{n_{\max}} \cos n\theta \tag{17}$$

Thin Plate Model

The governing differential equation for the thin plate model is given in Ref. 8:

$$\nabla^2\nabla^2 w = 0 \tag{18}$$

in which

$$\nabla^2 w \equiv w'' + w'/r + \ddot{w}/r^2 \tag{19}$$

where superscript prime indicates differentiation with respect to r and superscript dot indicates differentiation with respect to θ. The deflection of the thin circular plate due to a single concentrated load at $r=r_i$ is calculated by solution of this equation in the two regions $r \le r_i$ and $r \ge r_i$ and determination of coefficients by application of force and displacement continuity conditions at $r=r_i$ and boundary conditions at $r=r_0$.

The general solution of Eq. (18) is:

$$w = R_0 + \sum_{n=1}^{n_{\max}} R_n \cos n\theta \tag{20}$$

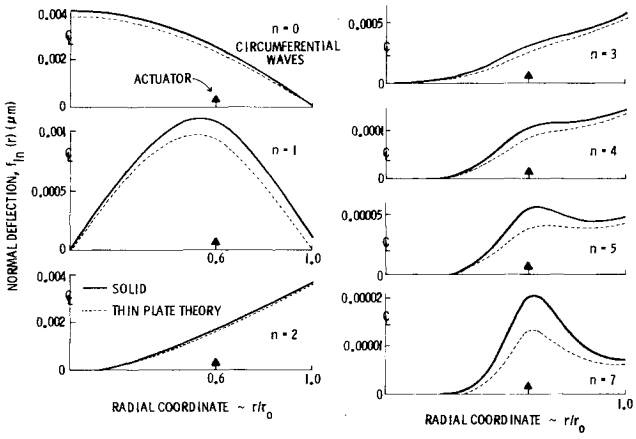

Fig. 4 Influence functions $f_{in}(r)$ for unit actuator load at $r_i/r_0 = 0.6$ generated from the thin plate model and the solid-of-revolution model.

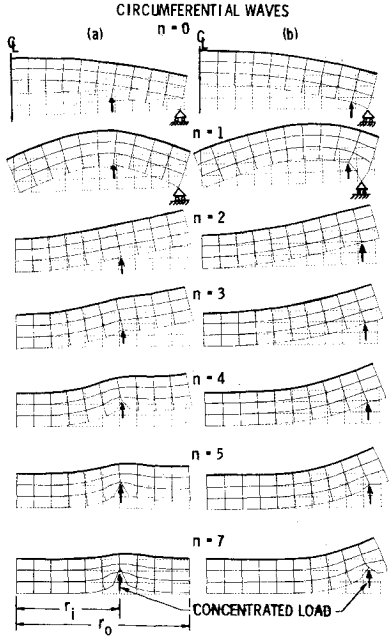

Fig. 5 Influence functions from the solid-of-revolution model for actuator band locations at a) $r_i/r_0 = 0.6$ and b) $r_i/r_0 = 0.9$.

in which

$$R_0 \equiv A_0 + B_0 \ell n(r) + C_0 r^2 + D_0 r^2 \ell n(r)$$

$$R_1 \equiv A_1 + B_1 r^{-1} + C_1 r^3 + D_1 r \ell n(r)$$

$$R_n \equiv A_n r^n + B_n r^{-n} + C_n r^{n+2} + D_n r^{-n+2} \quad (n \geq 2) \tag{21}$$

As the inner region $0 \leq r \leq r_i$ has no central hole, the solution $\bar{w}$ in that region simplifies to

$$\bar{w} = \bar{R}_0 + \sum_{n=1}^{n_{max}} \bar{R}_n \cos n\theta \tag{22}$$

in which

$$\bar{R}_0 \equiv \bar{A}_0 + \bar{C}_0 r^2; \quad \bar{R}_n \equiv \bar{A}_n r^n + \bar{C}_n r^{n+2} \tag{23}$$

At the radius $r = r_i$, the following continuity conditions must be satisfied

$$\bar{w} = w; \quad \bar{w}' = w'; \quad \bar{w}'' = w''; \quad \bar{Q} - Q_r = P_i(\theta) \tag{24}$$

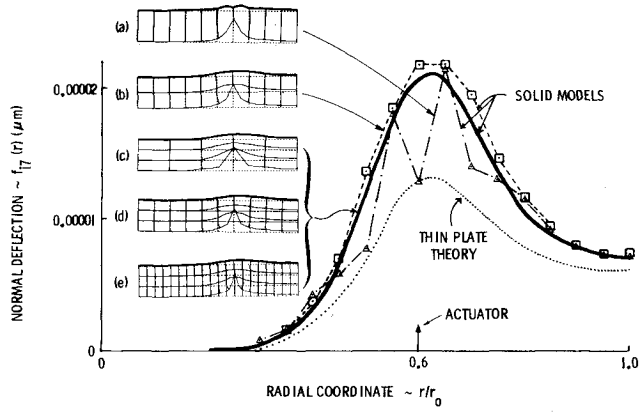

Fig. 6 Convergence of influence function $f_{i7}(r)$ for various finite-element discretizations.

Table 1 RMS mirror surface phase compensation error corresponding to commanded displacement shown in Fig. 3 and actuator distribution shown in Fig. 7

Case no.	Number of circumferential harmonics[a]	Structural model	rms normal displacement error, $\sqrt{E}$ [Eq. (4)], μm
1	0 ($w_a = 0$)	(Commanded distortion is independent of the structural model)	0.295
2	5	Thin plate theory	0.0254
3	6	Thin plate theory	0.0256
4	7	Thin plate theory	0.0266
5	10	Thin plate theory	0.02682
6	20	Thin plate theory	0.02686
7	10	Solid, 1 layer, as in Fig. 6a, with 2×2 Gaussian integration points in each element	0.02848
8	10	Same as Case 7, except 3×3 Gaussian points	0.02817
9	10	Same as Case 8, except 3 layers, as in Fig. 6d	0.02837

[a] $n_{max} + 1$, included in $w_a(r,\theta)$ [Eq. (2)].

$\bar{Q}_r$ and Q_r are the transverse shear force resultants given by

$$\bar{Q}_r = -K(\nabla^2 \bar{w}); \quad Q_r = -K(\nabla^2 w)' \tag{25}$$

where the quantity K is the plate bending stiffness.

At the edge $r = r_0$, the following boundary conditions are applied:

$$V_r = -K\left[(\nabla^2 w)' + \frac{1-\nu}{r^2}(\ddot{w}' - \ddot{w}/r)\right] = 0 \quad (n \geq 2) \tag{26a}$$

$$w = 0 \qquad (n = 0, 1) \tag{26b}$$

$$M_r = -K\left[w'' + \frac{\nu}{r}(w' + w''/r)\right] = 0 \quad \text{(all } n\text{)} \tag{26c}$$

in which V_r is the normal force resultant, M_r is the radial moment resultant, and ν is Poisson's ratio. The boundary condition Eq. (26b) is applied for $n = 0$ and $n = 1$ to prevent singularity corresponding to rigid body motions. The rigid body modes are considered to be additional influence functions, as described earlier. For unit actuator loads at $r_i < r_0$, the solution for each circumferential harmonic is given by Eqs. (20) and (23) with $\bar{A}_n, \bar{C}_n, A_n, B_n C_n, D_n$ being determined from the six conditions in Eqs. (24) and (26). For unit actuator loads at the edge $r_i = r_0$, the solution is given by Eq.

(23) alone, with the boundary condition Eq. (26a or b) replaced by

$$V_r = P_i(\theta) \quad (n \geq 2); \quad \bar{w} = 0 \quad (n = 0,1) \tag{27}$$

The influence functions $f(r)$, $i = 1,2,\ldots N$ in Eq. (2) consist of $\bar{w}_n$ and w_n.

Figure 4 shows influence functions for several circumferential harmonics corresponding to an actuator located at $r_i/r_0 = 0.6$. The comparison between the $f_{in}(r)$ predicted with the thin plate model and the less restrictive solid-of-revolution model will be discussed in the next section.

Solid-of-Revolution Model

The circular plate considered in the analysis and shown in Fig. 2 is rather thick. Therefore, application of thin plate theory yields somewhat inaccurate predictions. It is more accurate to perform the analysis summarized in Eqs. (1-8) with the use of influence functions derived from a model in which the deformations are not restricted by the assumptions of thin plate theory. Figure 5 shows influence functions for actuators located at $r_i/r_0 = 0.6$ and $r_i/r_0 = 0.9$ derived by a computer program BOSOR6.[9] The amplitudes of the distortion in the various circumferential harmonics are not plotted to the same scale. For example, the maximum unit load deflections for $n = 2$ are more than two orders-of-magnitude greater than those for $n = 7$, as seen in Fig. 4. The influence functions $f_{in}(r)$, $i = 1,2,\ldots N$ of Eq. (2) are the normal deflections of the upper surface indicated by the heavy lines in Fig. 5. The influence functions for $r_i/r_0 = 0.6$ are also shown in Fig. 4 where they are compared to those derived from the thin plate theory. The apparent overlapping of deformed elements for $n = 7$ and $r_i/r_0 = 0.6$ in Fig. 5 results from exaggeration of the displacement for pictorial representation.

The solid of revolution is modeled as an assemblage of isoparametric 8-node quadrilateral elements of revolution.[10] This element was chosen over the 4-node element because it does not yield spuriously stiff structural models in cases involving a relatively large amount of bending.

In the model shown in Fig. 5, the axial and circumferential displacement components are set equal to zero at the lower right-hand corner for $n = 0$ and $n = 1$. These conditions prevent singularity due to rigid body motion. They are analogous to the boundary condition Eq. (26b) for the thin plate model. As before, influence functions (3) corresponding to rigid body motion are added to the summation over i in Eq. (2).

Inspection of Fig. 4 shows that the influence functions from the more approximate thin plate model agree rather closely with those from the solid-of-revolution model for wave numbers less than 4. The larger discrepancy for the higher circumferential harmonics is not particularly significant in this case, because these harmonics are not present in the commanded distortion pattern shown in Fig. 3 and their amplitudes are much smaller than those corresponding to the lower harmonics, as indicated in Fig. 4. As expected, the unit load influence functions predicted with the use of the solid-of-revolution model are of higher amplitude than those predicted with the use of the thin plate model.

Figure 6 shows the results of a study of convergence with grid size for the influence function $f_{i7}(r)$ for $r_i/r_0 = 0.6$. Convergence for $n = 7$ is slower than that for lower harmonics because of the local nature of the distortions on the back surface in this relatively high harmonic. Since model (d) is clearly adequate for prediction of $f_{i7}(r)$, it is also adequate for prediction of $f_{in}(r)$ $n < 7$. It is seen from Table 1 that harmonics $n > 7$ are not required in this case to obtain an accurate calculation of the rms phase compensation error.

Comparison of Phase Compensation Error $E^{1/2}$ with Use of the Two Models

Table 1 lists the rms difference between the commanded and actuated surface for the actuator distribution shown in

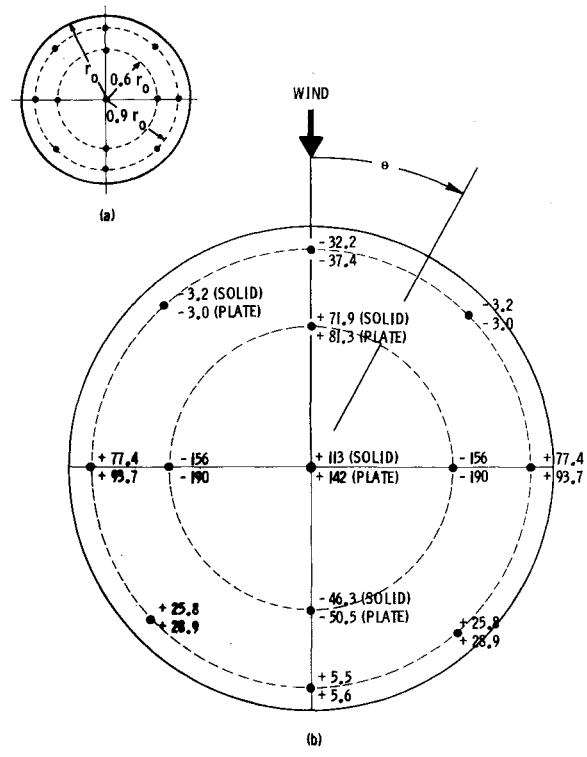

Fig. 7 a) Actuator locations and b) forces in newtons generated from the solid-of-revolution model and the thin plate model.

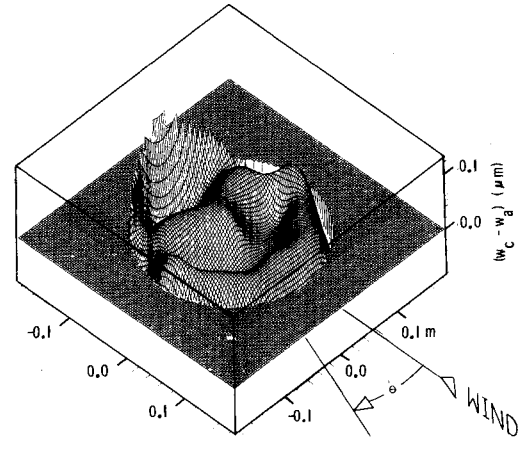

Fig.8 Distribution of phase compensation error $(w_c - w_a)$ corresponding to w_c as shown in Fig. 3 with actuators distributed as shown in Fig. 7.

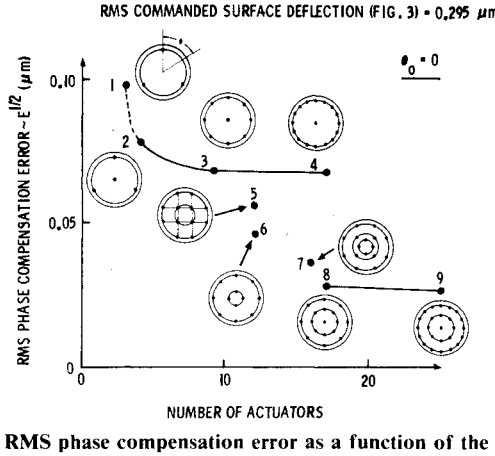

Fig. 9 RMS phase compensation error as a function of the number and distribution of actuators.

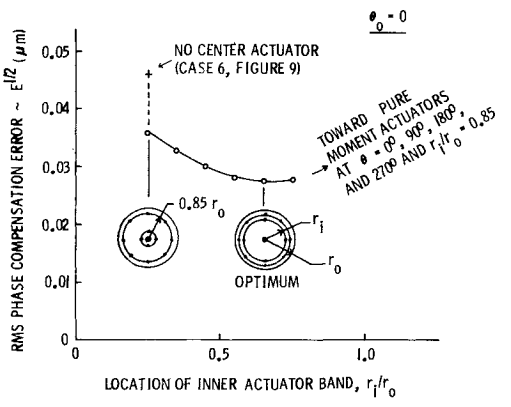

Fig. 10 Finding the optimum radius for the inner actuator band for actuators distributed in a 1-4-8 configuration.

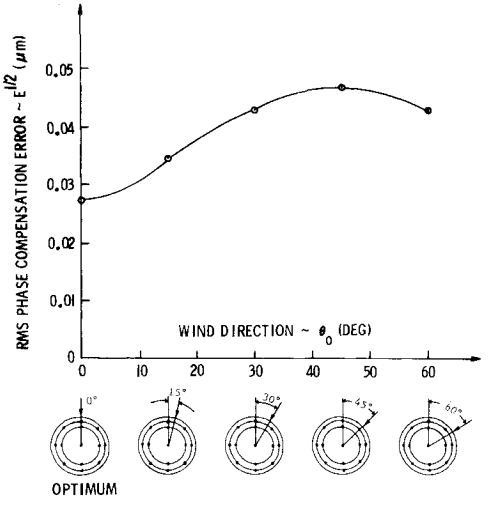

Fig. 11 RMS phase compensation error as a function of wind direction for the 1-4-8 configuration.

Fig. 7. Case 1 is included in order to give the rms difference between the commanded distortion $w_c(r,\theta)$ and the initially flat surface (no correction). Cases 2-6 list the results of a convergence study of $E^{1/2}$ with increasing n_{max}. They show that, with the use of thin plate theory, inclusion of only $n = 0,1,2,3,4$ yields accurate results. It is not possible to obtain a solution for $n_{max} < 4$ with the actuator distribution shown in Fig. 7 because the matrix A in Eq. (5) becomes singular if n_{max} is less than half of the maximum number of actuators located on any given circumference.

Cases 7-9 show that $E^{1/2}$ is not sensitive to the various solid-of-revolution models shown in Figs. 6a-e. The unit load surface deflections $f_{in}(r)$ predicted with use of 2×2 Gaussian integration points in each element are more jumpy than those obtained with use of 3×3 Gaussian points so that the structural model for Case 7 is not as suitable as that for Case 8, even though the average phase compensation error $E^{1/2}$ fortuitously happens to be closer to the converged value corresponding to the more refined model in Case 9. The converged rms phase compensation errors from the thin plate model and the solid-of-revolution model differ only by 5½%. The thin plate model is quite good for the prediction of rms phase compensation error as a function of number and location of actuators. Therefore this simpler, more economical, model was used for the parameter study described in the following section.

There are three reasons why thin plate theory is adequate in this case for prediction of phase compensation error as a function of number and placement of actuators:

1) The low circumferential harmonics ($n \leq 3$) are by far the most significant contributions to $w_a(r,\theta)$. For these harmonics, Figs. 4 and 5 show that the solid behaves essentially as a thin plate.

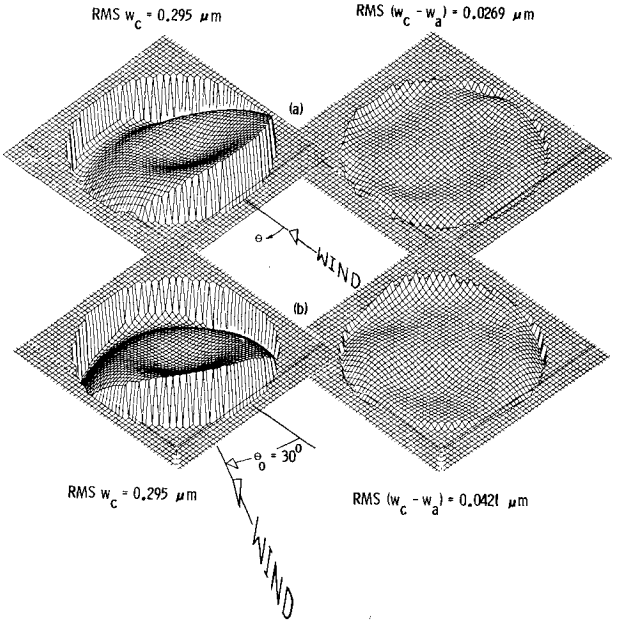

Fig. 12 Commanded phase compensation and phase compensation error for a case in which the actuators are distributed as shown in Fig. 7.

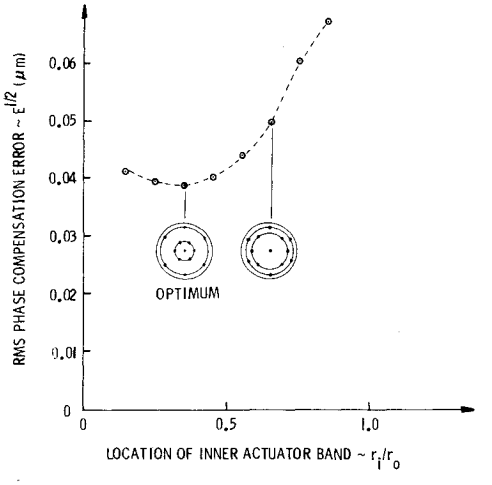

Fig. 13 Finding the optimum radius for the inner actuator band for actuators distributed in a 1-6-6 configuration.

2) For the higher harmonics, the thickness of the plate serves to smooth the normal displacement function. Even though the distortion as a whole cannot be predicted adequately with the use of thin plate theory, the normal displacement on the *mirror* surface, the influence function $f_{in}(r)$, is represented fairly well. Compare especially the surface influence functions $f_{i4}(r)$ plotted in Fig. 4 with the overall distortion for $n = 4$ plotted in Fig. 5a.

3) Much of the discrepancy between the influence functions for $n = 1$ shown in Fig. 4 is removed by rigid body tilt about the $\theta = 90$ deg diameter on the mirror surface.

However, note from Fig. 7b that the actuator *forces* predicted with use of the two structural models differ by as much as 25%. Hence, if thin plate theory is used to predict the actuator forces required to produce the commanded distortion with minimum rms error, the actual rms error in a real system will differ by more than the 5½% just cited. The 5½% difference would be achievable only for a closed-loop control system. Generally smaller forces are predicted for the solid-of-revolution model because it is more flexible, being free from the restrictions of thin plate theory.

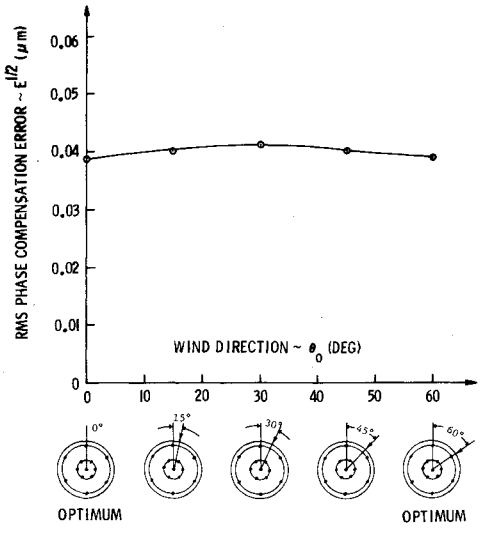

Fig. 14 RMS phase compensation error as a function of wind direction for the 1-6-6 configuration.

Figure 8 shows the difference in normal displacement $(w_c - w_a)$ with actuators placed as indicated in Fig. 7. Both structural models yield practically identical distributions of $(w_c - w_a)$.

rms Phase Compensation Error $E^{1/2}$ vs Number and Locations of Actuators

Once it has been determined that the computationally economical thin plate model is adequate for the calculation of rms phase compensation error, this model can be used in a parameter study to determine the most economical number and best locations of actuators. Figure 9 shows some results of such a study. The location of the outer band of actuators is fixed at $0.85\ r_0$. Experience[5] has shown that the outermost band should be as near the edge as possible, but the finite size of the actuators precludes their location from being exactly at the edge.

Trial configurations are numbered in Fig. 9. Case 1 represents the rms phase compensation error remaining after rigid body axial displacement and tilt about $\theta = 90$ deg. (Since there are only three actuators, the three force and moment equilibrium constraint conditions Eq. (8), dictate that all actuator forces a_i, $i = 1,2,3$ must be zero. Hence only rigid body phase compensation is possible in this case.) Cases 2-4 are connected by a solid line because they belong to a family—a configuration with a central actuator and one band at $r_i = 0.85\ r_0$. Similarly, cases 8 and 9 belong to a single family. It is seen from Fig. 9 that a centrally located actuator is useful, an inner band is beneficial, and little is gained by placing more than eight actuators on the outer band.

Figure 10 presents the results of a study in which the optimum location of the inner actuator band is sought. At first it may appear surprising that as the inner band approaches the outer band the rms phase compensation error $E^{1/2}$ does not approach the value obtained in case 3 of Fig. 9. This is because the four closely spaced pairs of actuators at $r_i = 0.85 r_0$ and $\theta = 0$, 90, 180, and 270 deg apply axial forces and meridional moments, whereas the similarly placed single actuators in case 3 of Fig. 9 apply only axial forces.

Figure 11 shows the variation in $E^{1/2}$ with wind direction for the optimum configuration of Fig. 10. The variation for the entire range 0 deg $\leq \theta_0 \leq 360$ deg can be constructed by appropriate reflections of the curve for $0 \leq \theta_0 \leq 45$ deg. Figure 12 shows w_c and $(w_c - w_a)$ to the same scale for $\theta_0 = 0$ and 30 deg. Figures 13 and 14 show results analogous to those in Figs. 10 and 11. The total number of actuators is the same, but the two bands each have 6 actuators rather than 4 and 8 as before. The rms error averaged over θ_0 is slightly higher in the 1-6-6 configuration than in the 1-4-8 configuration. However,

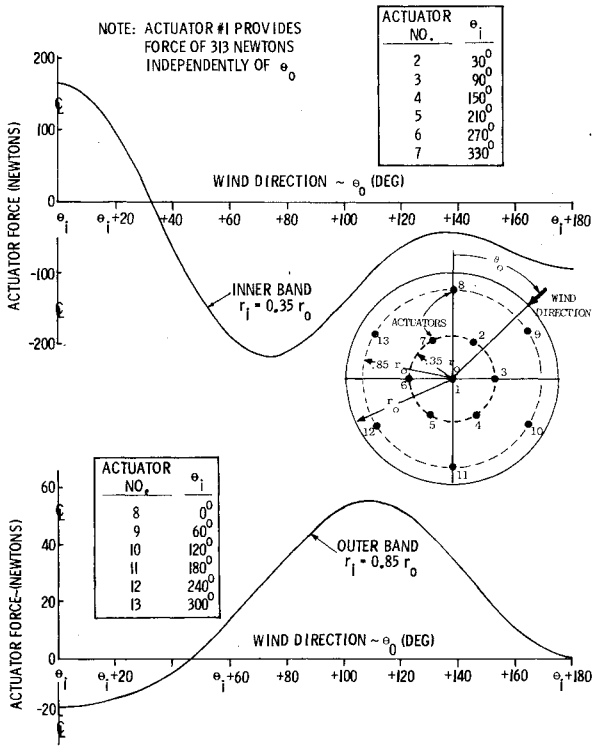

Fig. 15 Actuator forces predicted from the thin plate model for the 1-6-6 actuator configuration.

the quality of phase compensation in the former case is almost independent of wind direction. Hence, the 1-6-6 configuration is felt to be the better of the two.

All of the actuator forces in the 1-6-6 configuration for any wind direction can be determined from Fig. 15. The curves are symmetrical about the axis at $\theta_0 = \theta_i$.

Conclusions

In the example presented here, an objective has been to find the best number and optimum distribution of actuators required to impose a surface deformation on a rather thick circular mirror plate which reasonably closely approximates a commanded deformation that corrects for laser beam phase error due to thermal blooming. It was further desired to check the results obtained with use of thin plate theory by introduction of influence functions derived from a less restrictive but computationally more expensive structural model in which the mirror plate is treated as a deformable solid of revolution discretized with 8-node isoparametric elements of revolution.

For the geometry investigated, it is shown that the results of the optimization study for determination of the best number and location of actuators are not at all sensitive to the choice of structural model for the mirror. The predicted actuator forces are more sensitive to which structural model is used; the largest actuator force from the thin plate model being some 25% higher than that from the solid-of-revolution model. However, if the forces obtained from the thin plate model are applied to the solid-of-revolution model, the rms phase compensation error increases from 0.0286 μm to about 0.0320 μm, a change of only 11%. The rms phase compensation error is only mildly sensitive to changes in the actuator force distribution because much of the phase compensation is accomplished by rigid body axial displacement and tilt about $\theta = 90$ deg, as seen from case 1 in Fig. 9.

Similar studies carried out for mirrors of sandwich wall construction and for phase compensation in nonuniformly heated systems would be useful. Also, thin plate and solid-of-revolution models would doubtlessly yield increasingly different results in cases for which increasing phase correction

accuracy is desired. In such cases, the error contains an increasing magnitude of high spatial frequency components, as shown in Ref. 5. Thin plate and solid-of-revolution models yield increasingly different influence functions for higher circumferential harmonics, as shown in Figs. 4 and 6. Thus the discrepancy in rms errors from the two models would increase with the demand for increased accuracy of phase correction.

Acknowledgment

This research was sponsored by the 1978 Lockheed Independent Development Program. The authors are grateful to M. Waldman for his support and encouragement, to B. Almroth for his helpful comments, and to C. Miller for her art work.

References

[1] Bradley, L. C. and Hermann, J., "Phase Compensation for Thermal Blooming," *Applied Optics*, Vol. 13, Feb. 1974, pp. 331-334.

[2] Primmerman, C. A. and Fouche, D. G., "Thermal-Blooming Compensation: Experimental Observations Using a Deformable-Mirror System," *Applied Optics*, Vol. 15, April 1976, pp. 990-995.

[3] Hardy, J. W., "Active Optics: A New Technology for the Control of Light," *Proceedings of the IEEE*, Vol. 66, June 1978, pp. 651-697.

[4] Bushnell, D., "Control of Surface Configuration by Application of Concentrated Loads," *AIAA Journal*, Vol. 17, Jan. 1979, pp. 71-77.

[5] Bushnell, D., "Control of Surface Configuration of Nonuniformly Heated Shells," *AIAA Journal*, Vol. 17, Jan. 1979, pp. 78-84.

[6] Born, M. and Wolf, E., *Principles of Optices*, 2nd ed., Pergamon Press, New York, 1959, p. 465.

[7] Munn, M. W., Benson, R. S., Hendricks, W., Kohfeld, J. J., and Thoenes, J., "Optical Propagation Modeling for High Energy Laser Systems," LMSC-D566147, Vol. 1, Lockheed Missiles & Space Co., Inc., Dec. 1977, pp. 4-25 to 4-32.

[8] Timoshenko, S. and Woinowsky-Krieger, S., *Theory of Plates and Shells*, 2nd ed., McGraw-Hill, New York, 1959, pp. 282-291.

[9] Bushnell, D., "Stress, Buckling and Vibration of Hybrid Bodies of Revolution," *Computers & Structures*, Vol. 7, 1977, pp. 517-537.

[10] Zienkiewicz, O. C., "Isoparametric and Applied Numerically Integrated Elements—A Review," *Numerical and Computer Methods in Structural Mechanics*, Academic Press, New York, 1973, pp. 13-41.